Building Random Alloy Surfaces from Intermetallic Seeds: A General Route to Strain-Engineered Electrocatalysts with High Durability

Jocelyn T.L. Gamler,[1] Hannah A. Ashberry,[1] Xiahan Sang,[2] Raymond R. Unocic,[2] and Sara E. Skrabalak[1*]

[1] Department of Chemistry, Indiana University - Bloomington, 800 E. Kirkwood Ave. Bloomington, IN 47405.

[2] Center for Nanophase Materials Sciences, Oak Ridge National Laboratory, One Bethel Valley Road, Oak Ridge, Tennessee 37831 United States.

Correspondence and requests for materials should be addressed to S.E.S. (email: sskrabal@indiana.edu).

Abstract:

Pt-based catalysts are common in fuel cells but suffer from high cost and poor durability. To overcome these limitations, earth-abundant metals can be incorporated in core@shell architectures or through alloy formation. Here, the versatility of seed-mediated co-reduction (SMCR) is demonstrated with the deposition of PtM (where M = Ni, Co, Cu, or Fe) random alloyed shells on PdCu B2 intermetallic seeds, integrating the concepts of a core@shell architecture and alloyed surfaces into one nanostructure. Control of shell thickness and Pt:M ratios is demonstrated, providing a general route to strain-engineered alloyed surfaces. The performance of these nanocatalysts was evaluated for the oxygen reduction reaction (ORR) as a function of shell thickness and shell composition, where PtCu and PtNi shells showed highest activity and

outperformed PtCu and PtNi references. Significantly, this work demonstrates the versatility of SMCR as a facile way to control the many levers of catalyst design within one platform.

Developing catalysts for the oxygen reduction reaction (ORR) is challenging because the material must withstand highly corrosive environments and be chemically active enough to activate the O_2 bond but not readily form a metal-oxide layer.[1] Pt nanoparticles (NPs) are often used as the benchmark catalyst, but their large scale use is impractical due to cost. Compressively straining the Pt lattice through alloying or the lattice mismatch of core@shell architectures can weaken adsorbed hydroxyl and lead to enhanced activity for the ORR,[2] with both core@Pt[3,4,5] and PtM[6,7,8,9,10] NPs having been examined as ORR catalysts. Such structures result in destabilized adsorbed hydroxyl, which is otherwise a strongly bound intermediate in the ORR.[11,3] This destabilization, in turn, increases the rate of reaction. In the case of alloys, addition of transition metals such as Ni is promising.[10,12] However, Ni and other 3d transition metals are prone to dissolution in acidic media over long periods of time, although intermetallic phases have reported higher durability.[13,34,35]

Here, the versatility of seed-mediated co-reduction (SMCR) is demonstrated for the integration of a core@shell architecture, alloyed surfaces, and high-durability intermetallics into one NP platform. Core@shell NPs with highly strained multimetallic surfaces offer decreased noble metal loading and access to strained ensemble effects.[14] When built on intermetallic seeds, we recently showed that random alloyed surfaces can be stabilized to provide highly durable electrocatalysts.[36] However, little effort has been dedicated to developing general synthetic tools to achieve high quality nanomaterials that combine all of these features. SMCR is an attractive method to generate such nanomaterials as multimetallic surfaces can be deposited on a diversity

of seeds through the simultaneous reduction of multiple metal salts. To date, most work has focused on AuPd deposition on Au or Pd seeds for applications in plasmonics.[15] However, our group recently showed that random alloy PtCu shells in a 2:1 Pt:Cu ratio could be deposited on intermetallic PdCu B2 seeds, resulting in highly strained alloyed surfaces by SMCR.[16] These PdCu B2@PtCu NPs were an effective and highly durable ORR catalyst on account of the intermetallic interior.

Herein, the generality of SMCR as a route toward strain-engineered, highly durable nanocatalysts with tunable alloyed surfaces is demonstrated. Specifically, random alloy PtM shells (where M = Ni, Fe, Co, and Cu) with tunable Pt:M ratios and thicknesses were deposited on intermetallic PdCu B2 seeds by facile manipulation of the synthetic conditions, as depicted in Scheme 1. A systematic analysis of various PdCu B2@PtM nanocatalysts for the ORR was undertaken to elucidate how structural and compositional features impact performance. Overall, this study demonstrates that SMCR is a general route to strain-engineered alloyed nanocatalysts with high durability. We anticipate the design criteria outlined herein will enable new nanocatalysts to be accessed for a variety of reactions with simple changes in initial synthetic parameters.

Scheme 1. Overview of Synthetic Versatility of SMCR and the Parameters Controlled in This Study

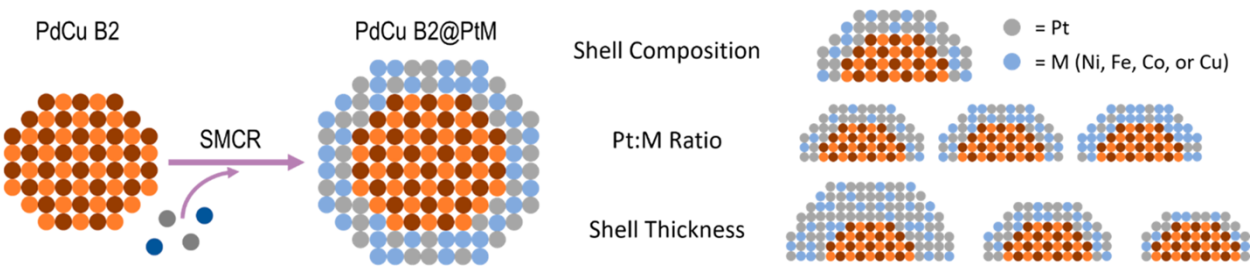

Experiment Methods:

Chemicals

Oleylamine (70%, OLA), oleic acid (90%, OA), trioctylphosphine (97%, TOP), 1,2-dodecanediol (90%, DDD), 1-octadecene (90%, ODE), dodecanthiol (DDT), platinum acetylacetonate ($Pt(acac)_2$), platinum bromide ($PtBr_2$), copper(II) acetate ($Cu(ac)_2$), palladium(II) bromide ($PdBr_2$), and copper acetylacetonate ($Cu(acac)_2$) were purchased from Aldrich and unaltered. Cobalt(II) acetate tetrahydrate ($Co(ac)_2{\cdot}4H_2O$), iron(II) chloride tetrahydrate ($FeCl_2{\cdot}4H_2O$), and perchloric acid solution ($HClO_4$, 1.0 M) were received from Sigma-Aldrich. Nickel acetylacetonate ($Ni(acac)_2$) was received from Strem Chemical. Nafion (LQ-1105-110 EW at 5%) was purchased from the Fuel Cell Store. Nanopure water (18.2 MΩ cm) was used for all electrochemical testing. All chemicals were used without further purification.

Preparation of PdCu B2 Seeds

The PdCu B2 seeds were synthesized as previously described from the Skrabalak group.[16] To a 100 mL round bottom flask, 0.100 mmol $Cu(ac)_2$, 0.100 mmol $PdBr_2$ and 9.0 mL of OLA and 10 μL OA were added, and this mixture was heated under vacuum to 110 C and held for 30 minutes with stirring. Then, 50 μL of TOP were added, and the solution was heated to 235 C under Ar and held at this temperature for 20 minutes. The solution was allowed to cool to room temperature naturally. Size selection was necessary to get sample monodispursity. The solution was transferred to a centrifuge tube along with 20 mL hexane. The solution was spun at 1733·*g* for 10 minutes to remove the larger particles. Then, the rest of the particles were precipitated out by acetone and collected by centrifugation at 13786·*g*. The particles were washed 3 times with a mixture of ethanol and hexane (5:1 vol). The particles were suspending in hexane for further use.

Preparation of PdCu B2@PtM

The PdCu seeds were added to a 100 mL round bottom flask containing 0.010 mmol $PtBr_2$, 0.010 mmol of either $Cu(acac)_2$, $Co(ac)_2{\cdot}4H_2O$, $FeCl_2{\cdot}4H_2O$, or $Ni(acac)_2$. 1,2-dodecandiol was added with a 20:1 DDD:[Pt+M] molar ratio ratio, 7.0 mL ODE and 2.0 mL OLA. This mixture was heated to 110 C under vacuum and held at that temperature for 30 minutes. The temperature was then increased to 235 C under Ar and was allowed to incubate for 25 minutes. The particles were cooled and collected as previously described. To acheive different NPs with different Pt:Ni ratios and shell thickness shown in **Figure 1**, the PdCu B2 seeds were masses and converted to moles of seeds using the expected molar mass (169.9 g/mol). The Pt:Ni molar ratios were then added in reported ratios (3:1, 1:1, and 1:3) and the shell thickness was increased by changing the molar ratio between the PdCu B2:[Pt+M] in a 2:1, 1:1, and 1:2 for columns 1, 2, and 3, respectively.

Preparation of PtM/C references:

PtCu polyhedra were synthesized similarly to what was reported by Xu and coworkers.[31] Briefly, 19.8 mg of $Pt(acac)_2$, 13.2 mg of $Cu(acac)_2$, and 101.2 mg of ddd were dissolved in 7.0 mL of ODE and heated to 110 °C under an Ar stream for 15 minutes. Then a mixture of ODE/OLA (0.308 mL of OLA and 1.29 mL of ODE) and a mixture of DDT/ODE (0.0082 mL DDT and 0.242 mL ODE) were injected into the reaction solution. The solution was heated to 230 °C and incubated for 20 minutes. The solution was then cooled to room temperature and washed as previously described.

PtM (M = Fe, Ni, and Co) NPs were synthesize similarly to those presented by Yu and coworkers.[32] Briefly, 0.25 mmol of $Pt(acac)_2$ and 0.25 mmol of $Fe(acac)_2$, $Cu(acac)_2$, or $Ni(acac)_2$ were dissolve in 20 mL of OLA. The temperature was increased to 280 °C and held for 1 hour. The flask was cooled to room temperature and the particles were collected by centrifugation and precipitations with ethanol.

Characterization:

All NPs were characterized on a JEOL JEM 1010 TEM which operated at 80 keV and images collected with a ROM CCD camera. TEM samples were drop-casted onto the TEM grid after the entire sample was washed 2-3 times as described. Additional characterization with STEM-EDX was completed with JEOL JEM 3200FS operating at 300 keV images taken with Gatan 4k x 4k Ultrascan 4000 camera and the EDX mapping was obtained using and Oxford INCA dispersive x-ray system interfaced with the JEOL JEM 3200FS. The TEM samples were prepared as describe above. The Pt:M ratios were determined by using an SEM (FEI Qunata 600F Environmental SEM operating at 30 kV with a spot size of 3) interfaced with an Oxford INCA energy dispersive x-ray detector. High-resolution STEM images were collected with an aberration corrected Nion UltraSTEM 100 (operating at 100kV). The power diffraction (XRD) was collected on a PANalytical Empyrean instrument with Cu Kα radiation and an X'Celerator linear strip detector. The size of the NPs was measured from TEM images with an automated MATLAB code and was based on the constrast difference between the NPs and the background, details can be found in the work reported by Harak *et. al*.[17]

Electrochemical Evaluation:

A Pine Rotating Disk electrode was used to collect ORR measurements, with AfterMath 1.3.7060 software. A typical three-electrode cell was used where the working electrode was glassy carbon (diameter 5.5 mm, area 0.238 cm^2), the reference electrode was Ag/AgCl (4 M KCl), and a Pt coil was used as the counter electrode. The conversion between Ag/AgCl and RHE was done using the following equation: $E_{RHE} = E_{AG/AgCl} + 0.059\ pH + E^{\circ}_{Ag/AgCl}$.

All NPs were evenly dispersed on a carbon support (Ketjen EC-600JD). The NPs were massed and then resuspended in 1 mL of hexane. The NPs were then added dropwise to a slurry

of the carbon support in 5 mL of acetone and 2.5 mL of hexane. The mass ratio between the NPs and carbon support was 1:1. Once the NPs were added, the solution was sonicated for 1 hour and then left to stir overnight. The solvents were then evaporated and the resulting catalyst dried in vacuum overnight. The working electrode was prepared by creating a 2 $mg*mL^{-1}$ ink solution of the catalysts, where the solution consisted of 1:3.98:0.020 volumetric ratio of isopropanol:H_2O:Nafion. The catalyst ink was sonicated for 30 mins, and 10 μL was dropcast onto the glassy carbon electrode and dried. The Pt loading was determined by using the metal ratios determined by SEM-EDX in combination with the catalyst preparation method (a 1:1 mass ratio of carbon support to nanocatalyst).

Normalization of the electrode by sweeping 200 times between 60 mV and 1200 mV vs. RHE was performed first to remove any excess surfactant or surface contamination. Hydrogen desorption experiment were used to determine the ESCA and were performed by cycling between 60 and 1000 mV vs. RHE in an Ar purged 0.1 M $HClO_4$ solution. The area under the hydrogen desorption peaks were measured and using a conversion factor of 210 μCcm^{-2} was converted to the active surface area. The value obtained was then normalized by the Pt loading on the electrode.

Linear sweep voltammetry (LSV) was performed in an O_2-saturated solution of 0.1 M $HClO_4$ between 60 to 1200 mV (vs. RHE) at a scan rate of 10 mV/s at 1600 RPM. The kinetic current was obtained by collecting LSV curves at several different rotation speeds (400, 900, 1600, 2025, 2500 RPM). The specific (normalized by surface area) and mass (normalized by Pt loading) were determined at 850 mV and 900 mV (vs. RHE).

CO-stripping experiments were conducted by purging a 0.1 M $HClO_4$ with CO gas while holding the open circuit potential for 30 minutes. After the potential hold, the solution was purged

with Ar for 30 minutes to removed excess CO gas. The CO-stripping curves were obtained by cycling between 60 and 1200 mV (vs. RHE) at a scan rate of 50 mV/s.

Tafel plots were obtained by calculating the kinetic current (I_K) on the basis of the following equation where I is the measured current and I_L is the limiting current (current measured at 0.4 V vs RHE):

$$I_K = \frac{I \times I_L}{I_L - I}$$

Results and Discussion

Control of Alloy Shell Thickness and Pt:M Ratio

Surface-adsorbate interactions can be tuned through shell thickness and composition.[17, 18,19,20] Thus, synthetic control over these features is critical to achieving high performance catalysts. Herein, PtNi shells were used as a model system to show modulation of shell thickness and Pt:Ni ratio in the final structures due to the high activities of PtNi surfaces for the ORR.[6,7,9] Specifically, monodisperse PdCu B2 intermetallic NPs were synthesized as previously reported and used as seeds for the deposition of PtNi shells (**Figure S1**).[16] Tunable PtNi shell thicknesses and compositions were achieved by varying the concentrations of platinum (II) bromide ($PtBr_2$) and nickel (II) acetylacetonate ($Ni(acac)_2$) that were co-reduced at 235 C in the presence of the seeds with 1,2-dodecandiol in a solution 1-octadecene (ODE) and oleylamine (OLA). Shown in **Figure 1** are the products obtained as a function of Pt:Ni molar precursor ratio (rows A, B, and C correspond to 3:1, 1:1, and 1:3 Pt:Ni, respectively) and total metal precursor concentration (columns 1, 2, and 3 correspond to a total metal precursor-to-seed molar ratio of 1:2, 1:1, to 2:1, respectively). Transmission electron microscopy (TEM) images show good monodispersity for all samples, with spheroidal NPs with core@shell architectures achieved (**Figure 1**). As expected, the shell thicknesses of the NPs increased across each row as the total amount of shell precursor

increased relative to the number of seeds in a synthesis (**Figure S2**). Energy dispersive X-ray spectroscopy (EDX) interfaced to a scanning electron microscope (SEM) was used to evaluate the bulk Pt:Ni ratios of the samples, denoted in the lower right insets of **Figure 1**. As samples within each row have the same Pt:Ni input ratio, the ratio should be maintained within a row. For example, samples in row A were prepared with an input molar ratio of Pt:Ni at 3:1, and the final products have similar Pt:Ni ratios, albeit enriched with Pt. Decreasing Pt:Ni ratios are evident going down a column, consistent with the input Pt:Ni ratios decreasing from 3:1, 1:1, and 1:3, respectively.

Samples A3 and C3 were characterized by powder X-ray diffraction (XRD) to verify the crystal phases and composition of the nanostructures (**Figure S3**). The XRD patterns showed reflections for the intermetallic seeds, indicating that the PdCu B2 phase was maintained upon shell deposition. The (111), (200), and (220) reflections for the random alloy face-centered cubic (fcc) PtNi shells also appear at their anticipated positions based on their compositions from SEM-EDX, with the peaks associated with sample C3 shifted to higher 2θ positions than those for sample A3 due to more Ni having been incorporated into the shells.

To determine the spatial distribution of the four metals in these NPs, scanning transmission electron microscopy (STEM)-EDX was used to analyze samples A3 and C3 (**Figure 3A** and **S4** respectively). The Pd and Cu signals are localized at the centers of the particles and the Pt and Ni at the exteriors of the particles. The line scans support core@shell architectures (**Figure S5A** and **S5** for samples A3 and C3, respectively). Particles from samples A1 and C1 were also evaluated by STEM-EDX, and similar results were obtained, but the samples have thinner shells as expected (**Figure S6**).

To further investigate the crystalline nature of these core@shell NPs, spherical aberration (C_s)-corrected high-angle annular dark-field STEM (HAADF-STEM) was used. HAADF-STEM

images were collected for the PdCu B2@PtNi NPs along three different crystallographic directions of the core: [110], [111], and [100] (**Figure 2**). The angle-to-plane relationships show that, to minimize interfacial energy and lattice mismatch, the PtNi {111} facets were deposited on the PdCu B2 {110} facets. The facet-dependent deposition extends to the other crystallographic directions as well, where the {200} facets of the FCC shells deposit on the {100} intermetallic facets. This finding is similar to the first demonstration of PdCu B2@PtCu nanocatalysts, showing that facet-dependent deposition extends to other PtM shells.[16]

Control of Pt-M Shell Composition

As the work with PtNi deposition on PdCu B2 seeds demonstrates, SMCR is a facile method for tuning shell thickness and the Pt:M ratio. As it turns out, SMCR is also well suited to deposit a variety of other alloyed surfaces on intermetallic seeds. Specifically, random alloys of PtM, where M = Co, Fe, and Cu, were also targeted. These compositions were selected as alloying Pt with 3d transition metals can enhance catalysis through geometric and ligand effects, where further enhancements could be realized by straining these surfaces through a core@shell architecture.[1,21] Using the same SMCR conditions that facilitated deposition of PtNi shells on PdCu B2 seed, random alloyed PtCo, PtCu, and PtFe shells were deposited on the PdCu B2 seeds (**Figure 3B-D**). The shell metal precursors were added in 1:1 mole ratios of Pt:M where the Co, Cu, and Fe sources were cobalt (II) acetate ($Co(ac)_2$), copper (II) acetylacetonate ($Cu(acac)_2$), and iron (II) chloride ($FeCl_2$), respectively. The SEM-EDX results show again that there is a Pt rich shell (**Figure 3E**) for all samples. Size histograms show that similar particle sizes were achieved across the three PtM samples (**Figure S7**).

The spatial distribution of elements within these multimetallic NPs was determined by STEM-EDX (**Figure 3**). PtM (M = Cu, Co, and Fe) is located on the exteriors of the particles and

Pd and Cu are located in the interiors. These core@shell architectures also are supported by line scan analysis (**Figure S5 B-D**). Powder XRD of these samples show peaks consistent with the PdCu B2 phase of the cores (**Figure S8**). The SEM-EDX Pt:M (M = Cu, Co, Fe) ratios were used as before to determine the alloyed reference pattern, assuming a random alloy FCC structure. The (111) peak is evident in the XRD patterns of all samples, but the expected (200) and (220) peaks are not as prominent. The lack of defined peaks can be attributed to the thin shells deposited on the surface of the NP as the height of each peak is related to the amount of material and typically decreases in intensity at larger 2θ positions.[22]

Catalytic Evaluation of PdCu B2@Pt-M NPs

Control of NP design parameters such as shell thickness and surface composition is important for optimized performance. Tuning shell thickness tunes the binding strength of intermediates, and compositional control of an alloyed surface can manipulate the intrinsic catalytic activity.[22–25,10] Pt shells and Pt alloy surfaces are highly active for the ORR due to geometric, ligand, and strain effects.[1] However, these catalysts are susceptible to dealloying and do not display the ideal surface binding conditions to reach the theoretical maximum on ORR volcano plots.[29–31] As we found previously, PdCu B2@PtCu NPs were effective catalysts for the ORR on account of the strained alloyed surfaces and durable intermetallic cores.[17,19] However, integrated control over multiple NP design parameters to tune the surface binding conditions was not demonstrated. Here, precise control of both shell thickness and surface composition was demonstrated, and the resulting surface binding conditions were evaluated. Moreover, the various B2@PtM (M = Ni, Co, Fe, or Cu) catalysts were evaluated for the ORR and their activities evaluated as a function of shell thickness and composition (**Figure 4**).

Catalytic Evaluation of Shell Thickness

Control over shell thickness allows for tuning of surface-adsorbate interactions as a function of shell thickness. First, the PdCu B2@PtNi NPs in row A (**Figure 1**) were tested for the ORR, allowing for an analysis as a function of shell thickness. Row A samples were selected as PtNi surfaces with a high ratio of Pt show a higher activity toward the ORR than PtNi surfaces with less Pt (e.g., rows B and C).[1,13] The NPs were loaded onto a carbon support (EC-600JD, Ketjen) and are denoted as [A1]/C, [A2]/C, and [A3]/C, herein (**Figure S9**). These NPs were compared to a PtNi/C NP reference with similar composition, although we do note slight structural differences which are unavoidable given differences in preparation (**Figure S10**).

Polarization curves were collected from samples in an O_2-saturated 0.1 M $HClO_4$ solution on a rotating disk electrode at 1600 RPM (**Figure 4A**). In the mixed diffusion and kinetic region (0.8-1.0 V vs. RHE), the half-wave potential ($E_{1/2}$) can be used to qualitatively evaluate catalytic activity, where a positively shifted $E_{1/2}$ indicates a better catalyst. [A2]/C and [A3]/C show similar $E_{1/2}$ (0.819 V and 0.822 mV, respectively), which were + 30 mV shifts compared to [A1]/C and a + 10 mV shift compared to the PtNi/C reference. The specific activities (the kinetic currents obtained from the Koutckey-Levich equation and normalized by the electrochemically active surface areas of the various catalysts determined by hydrogen desorption experiments, **Figure S11**) were [A3]/C > PtNi/C > [A1]/C > [A2]/C, with all row A samples performing better than the Pt reference (**Figure 4B**). The origin of this trend will be discussed within the context of CO-stripping measurements, but we note that Sample [A1]/C has approximately one monolayer coverage and samples with skins (or very thin shells) often show unique surface binding.[26,27] The mass activities (normalized by mass of Pt on the electrode) were decreasing [A2]/C > [A3]/C > [A1]/C >PtNi/C > Pt/C (**Figure 4C**). This finding is unsurprising as there is an increase in Pt content within the interiors of the particles which is inaccessible to adsorbates. As the mass activities are determined

by dividing the kinetic current by the mass of Pt on the electrode, sample [A1]/C has a more negatively shifted $E_{1/2}$ resulting in much lower kinetic current translating to a decreased mass activity at both 0.9 V and 0.85 V.

These results indicate that catalyst performance (or surface-adsorbate interaction) can be tuned by shell thickness; however, the *d*-band position cannot be directly probed. Thus, CO-stripping was implemented to qualitatively resolve the relative positions of the *d*-band center, which can be correlated to surface-adsorbate interaction strength.[15,16] Cyclic voltammograms were collected in a CO-saturated solution of 0.1 M $HClO_4$ (**Figure 4B**). More negatively shifted peak potentials correlate with easier removal of CO from the surface, and in turn, a weakening of surface-adsorbate interactions. Both [A1]/C and [A3]/C show similar peak potentials, but [A3]/C yields a higher current density, which corresponds with more surface-bound CO. Sample [A3]/C showed the highest specific activity likely because of the larger catalytically activity surface area. Both [A2]/C and [A3]/C show two separated peaks: one around 750 mV and another between 850 mV and 900 mV, suggesting two binding conditions that may be due to the facet-dependent deposition giving rise to different strains on different facets. Regardless, weaker surface-adsorbate interactions are usually coupled with an increase in catalytic activity for the ORR. Thus, it unsurprising that samples [A1]/C and [A3]/C, which have more negative CO stripping peak potentials than [A2]/C, show higher ORR activity. This outcome also suggests that the degree of compressive strain (- 5.4 % lattice mismatch, *see Supplementary Information for details*) at the PtNi surface changes as a function of shell thickness in unanticipated ways. Compared to a PtNi reference, introduction of compressive strain should weaken oxygenated intermediates to accelerate the rate of the ORR. However, the large strain that accompanies the thin-shelled samples [A1]/C and [A2]/C may be too much, effectively weakening the binding of oxygenated

intermediates too much and resulting in a decreased kinetic current. Yet, strain relaxation can occur as shell thickness increases and can account for optimized binding strength for the thicker-shelled [A3]/C sample.[17,30] In considering this logic, there is an inversion in performance for samples [A1]/C and [A2]/C. As previously mentioned, sample [A1]/C has approximately monolayer coverage, which can result in unique surface electronics and greater mixing of core@shell components, and these deviations may be the origin of the inversion.

Accelerated Durability Testing

As previously mentioned, the instability of Pt alloyed surfaces limits the long-term use of many nanocatalysts due to dealloying in the harsh operating environment. We recently demonstrated that the Pt alloyed surface can be stabilized when it is deposited on an intermetallic core.[17,19] The origin of the durability enhancement was probed by simulations, which found Pt atoms at the core−shell interface to be stabilized by the ordering of the Cu atoms. Notably, this stabilization was evident regardless of whether or not Pd migrated from the core to be incorporated into the shell. To demonstrate the versatility of enhanced durability for other alloyed surface, accelerated durability testing (ADT) was completed for the PtNi surfaces. While there are many ways to examine the durability of a catalyst, including online ICP-MS and testing in a full fuel cell configuration, we opted for repeated electrochemical cycling, which is a conventional method for half-reaction evaluation.[39] Accelerated durability testing (ADT) was completed for the [A3]/C sample and compared to the PtNi/C reference by cycling 10 000 times between 0.2 and 1.0 V vs RHE in O_2-saturated 0.1 M $HClO_4$ (**Figure S13**). The [A3]/C catalyst showed a minimal $E_{1/2}$ shift of −6 mV after ADT, whereas the PtNi/C reference showed a −50 mV $E_{1/2}$ shift (**Figure S13C**). After 10 000 cycles, there was only a 17% activity decrease for the [A3]/C catalyst, but the activity for the PtNi/C sample decreased by 73%. SEM-EDX was used to evaluate the Pt:Ni atomic ratio

of both catalysts before and after ADT shown in **Table S1**. There is a small change in the Pt:Ni ratio for the [A3]/C sample from 5.0:1 to 6.4:1, demonstrating little change in the overall Ni content of the catalysts after 10 000 cycles. In contrast, there is a large change in the Pt:Ni ratio for the PtNi/C catalysts (2.9:1 before ADT and 13.1:1 after ADT), indicating that there is substantial Ni loss during catalysis. It is important to note that the Pd and Cu contents of the core@shell catalysts remained relatively unchanged (**Table S1**). While the initial activities of the core@shell catalyst and the bimetallic reference are similar, it is clear that after ADT the core@shell catalyst maintains its activity and composition better than the simple bimetallic reference. The increased stability of the core@shell catalyst is in agreement with other studies reported previously by our group.[17,19]

Catalytic Evaluation of Surface Composition

Though Pt alloy surfaces are closer to the peak of the ORR volcano plot than monometallic Pt catalysts, the theoretical maximum is still not accessed with current catalysts. Use of strain and ligand effects to enhance catalytic performance through alloy formation and implementation of core@shell structures is promising.[1] One can imagine that appropriately straining a surface of low activity could shift it toward the top of the volcano, while straining a highly active surface could decrease activity as a result of changes in the surface-adsorbate interactions.[10,1] Thus, deposition of PtM (M = Ni, Co, Fe, or Cu) shells on PdCu B2 seeds should lead to changes in catalytic performance when compared to bimetallic NPs with the same composition as the shells but without the core@shell architecture. Shown in **Figure 4D** are polarization curves for carbon-supported B2@PtM where M = Co, Fe, and Cu (i.e., Samples B2@PtCo/C, B2@PtFe/C, and B2@PtCu/C). The specific activities of these core@shell catalysts increased as B2@PtCo/C ~ B2@PtFe/C < B2@PtNi/C < < B2@PtCu/C (**Figure 4E,F**, respectively). Sample [A2]/C was used for

comparison to maintain a similar shell thickness across the different compositions. These were compared to a Pt/C reference (20 wt % Pt, Fuel Cell Store) and all core@sPtM catalysts showed higher activity than the Pt reference. We have also included for reference the PdCu B2 catalysts with no shell from a previous study and a monometallic Pt shell structure (**Figure S14**).[37] The decrease in activity of the normally highly active PtCo and PtFe surfaces can be attributed to the addition of lattice deformations (compressive or tensile, respectively) from the core@shell architecture, which causes non-ideal binding conditions. This estimated lattice deformation results from a difference in lattice mismatch between core and shell lattice constants. The degree of mismatch reported here was calculated by determining the mismatch between the nearest neighbor distances. The nearest neighbor distances were calculated using Vegard's law and the atomic ratios determined by EDX (**Figure S12**).

Again, CO-stripping was implemented to evaluate the surface-adsorbate interaction (**Figure S11E**). The Pt/C reference shows a large broad peak that encompasses all other CO-stripping peaks from the other core@shell catalysts. The peak potentials for the core@shell catalysts of different shell compositions increase from B2@PtNi/C < B2@PtCu/C < B2@PtFe/C < B2@PtCo/C. Similar to the thicker shells of PdCu B2@PtNi/C ([A2]/C and [A3]/C), the PdCu B2@PtCu/C catalysts exhibited two distinct peaks. The first peak is significantly more negative than all other CO-stripping peaks, indicating a weaker surface-adsorbate interaction, which could be the explanation for the increased ORR activity for PdCu B2@PtCu/C.

Integration of Concepts

Surface binding can be probed by several electrochemical methods. In the previous sections, CO-stripping and ORR catalysis were used to demonstrate predictive tuning of surface−adsorbate interactions by SMCR. **Figure 5** presents a summary of the electrochemical

results thus far. These results are summarized as a function of shell thickness in **Figure 5A**, where the plots for specific and mass activity intersect at an average shell thickness of about 0.6 nm, which would correspond to 3-5 monolayers (MLs) depending on the exposed facet. This intersection indicates a shell thickness that would optimize both specific and mass activity.

The addition of lattice strain to the bimetallic surface can be shown by comparing the catalytic activity from the core@shell NPs with varying surface compositions. As changes in composition are inherently accompanied by changes in strain in these core@shell systems, the different shell compositions were compared to bimetallic PtM (M = Ni, Cu, Co, or Fe) NP references with similar Pt:M ratios to the shells (**Figure S10**) supported on carbon (**Figure S15**), which provided different strain profiles (*i.e.*, core@shell architecture versus not). The electrochemical evaluation and comparison are shown in **Figures S16** and **S17**, respectively, with the PtM references giving similar performance to those reported in the literature with similar compositions (**Table S2**).[8,16,38] For both PtCo and PtFe surfaces, there is a decrease in catalytic activity when the alloyed surface is strained through the core@shell architecture. Due to the large lattice mismatch between bimetallic surface and core, intermediates would be bound inappropriately (too strongly for B2@PtFe/C and too weakly for B2@PtCo/C) for the ORR. For PtNi and PtCu surfaces, there is an increase in catalytic activity when the bimetallic surface is strained. For maximum activity, the surface-adsorbate interaction must be "just right". Our results show that straining a surface may cause the surface-adsorbate interaction to be too weak, too strong, or just right, and the effect can be tuned through core@shell composition, shell composition, and core@shell architecture. These catalytic results are summarized in **Figure 5B**, where the change in activity from a bimetallic reference to the core@shell catalyst is shown as a function of lattice mismatch. Although the catalytic activities are not among the best reported for

the ORR, the indispensable ability to tune the surface-adsorbate interaction in a predictable way is paramount to the advancement of the field.

Another useful analysis to probe changes in surface binding conditions is the Tafel analysis. Tafel plots reveal a change in the ORR rate-limiting step when incorporating a core@shell structure (**Figure S18**). The Tafel slope is relatively consistent for the PtM (M = Co, Ni, Cu, or Fe) references and close to −111 mV dec^{-1} corresponding to a first-electron reduction as the rate-limiting step, consistent with the literature for Pt alloy surfaces.[39] When lattice strain is introduced with the core@shell structure, there is a larger change in the Tafel slope. For all core@shell catalysts the Tafel slope was approximately −89 mV dec^{-1} indicating a change in the rate-limiting step.[40] Fundamentally this tells us that there is a change in the elementary steps for the ORR when the alloyed surface experiences compressive or tensile strain, thus supporting the facile manipulation of surface-adsorbate interactions.

Conclusions:

SMCR was shown to be a versatile method to deposit a variety of random alloy PtM shells on intermetallic seeds, with precise control over several nanocatalyst design parameters in one synthetic platform. These advances are summarized as follows. (1) *SMCR is a versatile route for depositing various alloyed surfaces on seeds*. This work shows that SMCR accommodates large degrees of lattice mismatch to introduce both compressive and tensile strain as a function of PtM identity and Pt:M ratio. (2) *Shell thickness can be predictably controlled via SMCR to tune surface-adsorbate interactions*. Using PdCu B2@PtNi NPs as a model system, shell thickness was controlled through simple manipulation of the shell metal precursor concentrations. Electrochemical evaluation of samples with varying shell thicknesses shows predicable tuning of activity. (3) *Alloyed surface can be stabilized by intermetallic cores*. This work shows that the use

of intermetallic cores to stabilize random alloyed surfaces is a generalizable concept. Specifically, PtNi surfaces deposited on the intermetallic cores showed enhanced durability when compared to a PtNi reference. Also shown with the PtCu surface, this generalizable feature advances the design of highly durable electrocatalysts. (4) *The Pt:M ratio can predictably be controlled with SMCR to tune surface-adsorbate interactions*. The Pt:M ratio determines active site density and ligand effects. While only demonstrated with the PdCu B2@PtNi model system, we note that one could imagine tuning the Pt:M ratios in the shell to achieve more active ORR surfaces for other surface compositions. In fact, our prior report of PdCu B2@PtCu NPs where the Pt:Cu ratio was 2:1 showed a greater than 10× increase in activity at 0.9 V versus RHE compared to the PdCu B2@PtCu NPs in this paper with a 1:1 ratio.[16] As PtM catalysts often have the highest activity when the Pt:M ratio is approximately 3:1, additional optimization should bring greater performance.[10] However, that optimization is not the focus of this paper. (5) *SMCR allows for each of these design parameters outlined in items 1-4 to be integrated into one nanostructure platform*. The versatility of SMCR established in this work demonstrates precise and facile synthetic control over many nanocatalyst design parameters within one synthetic platform, which is the key to efficiently tuning the surface-adsorbate interaction to enhance catalytic performance. We imagine that this synthetic method is applicable to other seed-growth techniques and can be used to readily achieve future high-performance catalysts. Of particular interest would be the identification of completely earth-abundant intermetallic cores which could impart high activity and durability, particularly as the cost of Pd is increasing and at times exceeding that of Pt.[41]

Data availability

All relevant data are available from the authors on request.

References

1. Greeley, J., Stephens, I. E. L., Bondarenko, A. S., Johansson, T. P., Hansen, H. A., Jaramillo, T. F., Rossmeisl, J., Chorkendorff, I. & Nørskov, J. K. Alloys of platinum and early transition metals as oxygen reduction electrocatalysts. *Nat. Chem.* **1,** 552–556 (2009).
2. Nørskov, J. K., Rossmeisl, J., Logadottir, A., Lindqvist, L., Kitchin, J. R., Bligaard, T. & Jónsson, H. Origin of the Overpotential for Oxygen Reduction at a Fuel-Cell Cathode. *J. Phys. Chem. B* **108,** 17886–17892 (2004).
3. Park, J., Zhang, L., Choi, S.-I., Roling, L. T., Lu, N., Herron, J. A., Xie, S., Wang, J., Kim, M. J., Mavrikakis, M. & Xia, Y. Atomic Layer-by-Layer Deposition of Platinum on Palladium Octahedra for Enhanced Catalysts toward the Oxygen Reduction Reaction. *ACS Nano* **9,** 2635–2647 (2015).
4. Choi, R., Choi, S.-I., Choi, C. H., Nam, K. M., Woo, S. I., Park, J. T. & Han, S. W. Designed Synthesis of Well-Defined Pd@Pt Core–Shell Nanoparticles with Controlled Shell Thickness as Efficient Oxygen Reduction Electrocatalysts. *Chem. – Eur. J.* **19,** 8190–8198 (2013).
5. Xiong, Y., Shan, H., Zhou, Z., Yan, Y., Chen, W., Yang, Y., Liu, Y., Tian, H., Wu, J., Zhang, H. & Yang, D. Tuning Surface Structure and Strain in Pd–Pt Core–Shell Nanocrystals for Enhanced Electrocatalytic Oxygen Reduction. *Small* **13,** 1603423 (2016).
6. Bu, L., Ding, J., Guo, S., Zhang, X., Su, D., Zhu, X., Yao, J., Guo, J., Lu, G. & Huang, X. A General Method for Multimetallic Platinum Alloy Nanowires as Highly Active and Stable Oxygen Reduction Catalysts. *Adv. Mater.* **27,** 7204–7212 (2015).
7. Chattot, R., Asset, T., Bordet, P., Drnec, J., Dubau, L. & Maillard, F. Beyond Strain and Ligand Effects: Microstrain-Induced Enhancement of the Oxygen Reduction Reaction Kinetics on Various PtNi/C Nanostructures. *ACS Catal.* **7,** 398–408 (2017).

8. Loukrakpam, R., Luo, J., He, T., Chen, Y., Xu, Z., Njoki, P. N., Wanjala, B. N., Fang, B., Mott, D., Yin, J., Klar, J., Powell, B. & Zhong, C.-J. Nanoengineered PtCo and PtNi Catalysts for Oxygen Reduction Reaction: An Assessment of the Structural and Electrocatalytic Properties. *J. Phys. Chem. C* **115,** 1682–1694 (2011).
9. Bu, L., Shao, Q., E, B., Guo, J., Yao, J. & Huang, X. PtPb/PtNi Intermetallic Core/Atomic Layer Shell Octahedra for Efficient Oxygen Reduction Electrocatalysis. *J. Am. Chem. Soc.* **139,** 9576–9582 (2017).
10. Stamenkovic, V. R., Mun, B. S., Arenz, M., Mayrhofer, K. J. J., Lucas, C. A., Wang, G., Ross, P. N. & Markovic, N. M. Trends in electrocatalysis on extended and nanoscale Pt-bimetallic alloy surfaces. *Nat. Mater.* **6,** 241–247 (2007).
11. Strasser, P., Koh, S., Anniyev, T., Greeley, J., More, K., Yu, C., Liu, Z., Kaya, S., Nordlund, D., Ogasawara, H., Toney, M. F. & Nilsson, A. Lattice-strain control of the activity in dealloyed core–shell fuel cell catalysts. *Nat Chem* **2,** 454–460 (2010).
12. Niu, G., Zhou, M., Yang, X., Park, J., Lu, N., Wang, J., Kim, M. J., Wang, L. & Xia, Y. Synthesis of Pt–Ni Octahedra in Continuous-Flow Droplet Reactors for the Scalable Production of Highly Active Catalysts toward Oxygen Reduction. *Nano Lett.* **16,** 3850–3857 (2016).
13. Choi, S.-I., Xie, S., Shao, M., Odell, J. H., Lu, N., Peng, H.-C., Protsailo, L., Guerrero, S., Park, J., Xia, X., Wang, J., Kim, M. J. & Xia, Y. Synthesis and Characterization of 9 nm Pt–Ni Octahedra with a Record High Activity of 3.3 A/mgPt for the Oxygen Reduction Reaction. *Nano Lett.* **13,** 3420–3425 (2013).
14. Liu, H., Nosheen, F. & Wang, X. Noble metal alloy complex nanostructures: controllable synthesis and their electrochemical property. *Chem. Soc. Rev.* **44,** 3056–3078 (2015).

15. Weiner, R. G., Kunz, M. R. & Skrabalak, S. E. Seeding a New Kind of Garden: Synthesis of Architecturally Defined Multimetallic Nanostructures by Seed-Mediated Co-Reduction. *Acc. Chem. Res.* **48,** 2688–2695 (2015).
16. Wang, C., Sang, X., Gamler, J. T. L., Chen, D. P., Unocic, R. R. & Skrabalak, S. E. Facet-Dependent Deposition of Highly Strained Alloyed Shells on Intermetallic Nanoparticles for Enhanced Electrocatalysis. *Nano Lett.* **17,** 5526–5532 (2017).
17. Harak, E. W., Koczkur, K. M., Harak, D. W., Patton, P. & Skrabalak, S. E. Designing Efficient Catalysts through Bimetallic Architecture: Rh@Pt Nanocubes as a Case Study. *ChemNanoMat* **3,** 815–821
18. Laskar, M. & Skrabalak, S. E. A balancing act: manipulating reactivity of shape-controlled metal nanocatalysts through bimetallic architecture. *J. Mater. Chem. A* **4,** 6911–6918 (2016).
19. Tang, Y. & Cheng, W. Key parameters governing metallic nanoparticle electrocatalysis. *Nanoscale* **7,** 16151–16164 (2015).
20. Xu, D., Bliznakov, S., Liu, Z., Fang, J. & Dimitrov, N. Composition-Dependent Electrocatalytic Activity of Pt-Cu Nanocube Catalysts for Formic Acid Oxidation. *Angew. Chem.* **122,** 1304–1307 (2010).
21. Asano, M., Kawamura, R., Sasakawa, R., Todoroki, N. & Wadayama, T. Oxygen Reduction Reaction Activity for Strain-Controlled Pt-Based Model Alloy Catalysts: Surface Strains and Direct Electronic Effects Induced by Alloying Elements. *ACS Catal.* **6,** 5285–5289 (2016).
22. Wang, G., Guan, J., Xiao, L., Huang, B., Wu, N., Lu, J. & Zhuang, L. Pd skin on AuCu intermetallic nanoparticles: A highly active electrocatalyst for oxygen reduction reaction in alkaline media. *Nano Energy* **29,** 268–274 (2016).

23. Cui, C., Gan, L., Heggen, M., Rudi, S. & Strasser, P. Compositional segregation in shaped Pt alloy nanoparticles and their structural behaviour during electrocatalysis. *Nat Mater* **12,** 765–771 (2013).
24. L. Stephens, I. E., S. Bondarenko, A., Grønbjerg, U., Rossmeisl, J. & Chorkendorff, I. Understanding the electrocatalysis of oxygen reduction on platinum and its alloys. *Energy Environ. Sci.* **5,** 6744–6762 (2012).
25. Greeley, J. & Nørskov, J. K. Combinatorial Density Functional Theory-Based Screening of Surface Alloys for the Oxygen Reduction Reaction. *J. Phys. Chem. C* **113,** 4932–4939 (2009).
26. Greeley, J. & Mavrikakis, M. Alloy catalysts designed from first principles. *Nat. Mater.* **3,** 810–815 (2004).
27. Xin, H. & Linic, S. Communications: Exceptions to the d-band model of chemisorption on metal surfaces: The dominant role of repulsion between adsorbate states and metal d-states. *J. Chem. Phys.* **132,** 221101 (2010).
28. Hammer, B., Nielsen, O. H. & Nrskov, J. K. Structure sensitivity in adsorption: CO interaction with stepped and reconstructed Pt surfaces. *Catal. Lett.* **46,** 31–35 (1997).
29. Jiang, T., Mowbray, D. J., Dobrin, S., Falsig, H., Hvolbæk, B., Bligaard, T. & Nørskov, J. K. Trends in CO Oxidation Rates for Metal Nanoparticles and Close-Packed, Stepped, and Kinked Surfaces. *J. Phys. Chem. C* **113,** 10548–10553 (2009).
30. Sneed, B. T., Young, A. P. & Tsung, C.-K. Building up strain in colloidal metal nanoparticle catalysts. *Nanoscale* **7,** 12248–12265 (2015).

31. Xu, D., Liu, Z., Yang, H., Liu, Q., Zhang, J., Fang, J., Zou, S. & Sun, K. Solution-Based Evolution and Enhanced Methanol Oxidation Activity of Monodisperse Platinum–Copper Nanocubes. *Angew. Chem. Int. Ed.* **48,** 4217–4221 (2009).

32. Yu, Y., Yang, W., Sun, X., Zhu, W., Li, X.-Z., Sellmyer, D. J. & Sun, S. Monodisperse MPt (M = Fe, Co, Ni, Cu, Zn) Nanoparticles Prepared from a Facile Oleylamine Reduction of Metal Salts. *Nano Lett.* **14,** 2778–2782 (2014).

33. Accuracy, Precision and Detection Limits | MyScope. at <http://www.ammrf.org.au/myscope/analysis/eds/accuracy/>

34. Wang, D., Xin, H. L., Hovden, R., Wang, H., Yu, Y., Muller, D. A., DiSalvo, F. J., Abruña, H. D. Structurally Ordered Intermetallic Platinum-Cobalt Core-Shell Nanoparticles with Enhanced Activity and Stability as Oxygen Reduction Electrocatalysts. *Nat. Mater.* **12,** 81–87 (2013).

35. Liu, H., Dou, M., Wang, F., Liu, J., Ji, J., Li, Z. Ordered Intermetallic PtFe@Pt Core-Shell Nanoparticles Supported on Carbon Nanotubes with Superior Activity and Durability as Oxygen Reduction Reaction Electrocatalysts. *RSC Adv.* **5,** 66471–66475 (2015).

36. Gamler, J. T. L., Leonardi, A., Ashberry, H. M., Daanen, N. N., Losovyj, Y., Unocic, R. R., Engel, M., Skrabalak, S. E. Achieving Highly Durable Random Alloy Nanocatalysts through Intermetallic Cores. *ACS Nano* **13,** 4008–4017 (2019).

37. Wang, C., Chen, D. P., Sang, X., Unocic, R. R., Skrabalak, S. E. Size-Dependent Disorder–Order Transformation in the Synthesis of Monodisperse Intermetallic PdCu Nanocatalysts. *ACS Nano* **10,** 6345–6353 (2016).

38. Li, X., An, L., Wang, X., Li, F., Zou, R., Xia, D. Supported Sub-5nm Pt–Fe Intermetallic Compounds for Electrocatalytic Application. *J. Mater. Chem.* **22,** 6047–6052 (2012).

39. Hu, P., Song, Y., Chen, L., Chen, S. Electrocatalytic Activity of Alkyne-Functionalized AgAu Alloy Nanoparticles for Oxygen Reduction in Alkaline Media. *Nanoscale* **7,** 9627–9636 (2015).

40. Shinagawa, T., Garcia-Esparza, A. T., Takanabe, K. Insight on Tafel Slopes from a Micokinetic Analysis of Aqueous Electrocatalysis for Energy Conversion. *Sci. Rep.* **5,** 13801 (2015).

41. Sun, J.-S., Wen, Z., Han, L.-P., Chen, Z.-W., Lang, X.-Y., Jiang, Q. Nonprecious Intermetallic Al7Cu4Ni Nanocrystals Seamlessly Integrated in Freestanding Bimodal Nanoporous Copper for Efficient Hydrogen Evolution Catalysis. *Adv. Funct. Mater.* **28,** 1706127 (2018).

42. Xu, Q., Chen, W., Yan, Y., Wu, Z., Jiang, Y., Li, J., Bian, T., Zhang, H., Wu, J., Yang, D. Multimetallic AuPd@Pd@Pt Core-Interlayer-Shell Icosahedral Electrocatalysts for Highly Efficient Oxygen Reduction Reaction. *Sci. Bull.* **63,** 494–501 (2018).

43. van der Vliet, D. F., Wang, C., Li, D., Paulikas, A. P., Greeley, J., Rankin, R. B., Strmcnik, D., Tripkovic, D., Markovic, N. M., Stamenkovic, V. R. Unique Electrochemical Adsorption Properties of Pt-Skin Surfaces. *Agnew. Chem., Int. Ed.* **51,** 3139–3142 (2012).

44. Baldizzone, C., Gan, L., Hodnik, N., Keeley, G. P., Kostka, A., Heggen, M., Strasser, P., Mayrhofer, K. J. J. Stability of Dealloyed Porous Pt/Ni Nanoparticles. *ACS Catal.* **5,** 5000–5007 (2015).

Acknowledgements

We acknowledge financial support from Indiana University and U.S. DOE BES Award DE-SC0018961. Access to the powder diffractometer provided by NSF CRIF CHE-1048613 and to

the XPS by NSF MRI DMR-1126394. We also want to thank the IU Electron Microscopy Center and Nanoscale Characterization Facility for access to the necessary instrumentation. Aberration-corrected STEM was conducted as part of a user proposal at Oak Ridge National Laboratory's Center for Nanophase Materials Sciences, a U.S. Department of Energy Office of Science User Facility (X.S. and R.R.U.)

Author Contributions

S.S. conceived and supervised the research. J.G designed and conducted experiments. J.G conducted most of data analysis. H.A collected XRD. X.S and R.R.U. collected HAADF-STEM images. All authors discussed the results and commented on the manuscript.

Competing Interests

The authors declare that they have no competing interests.

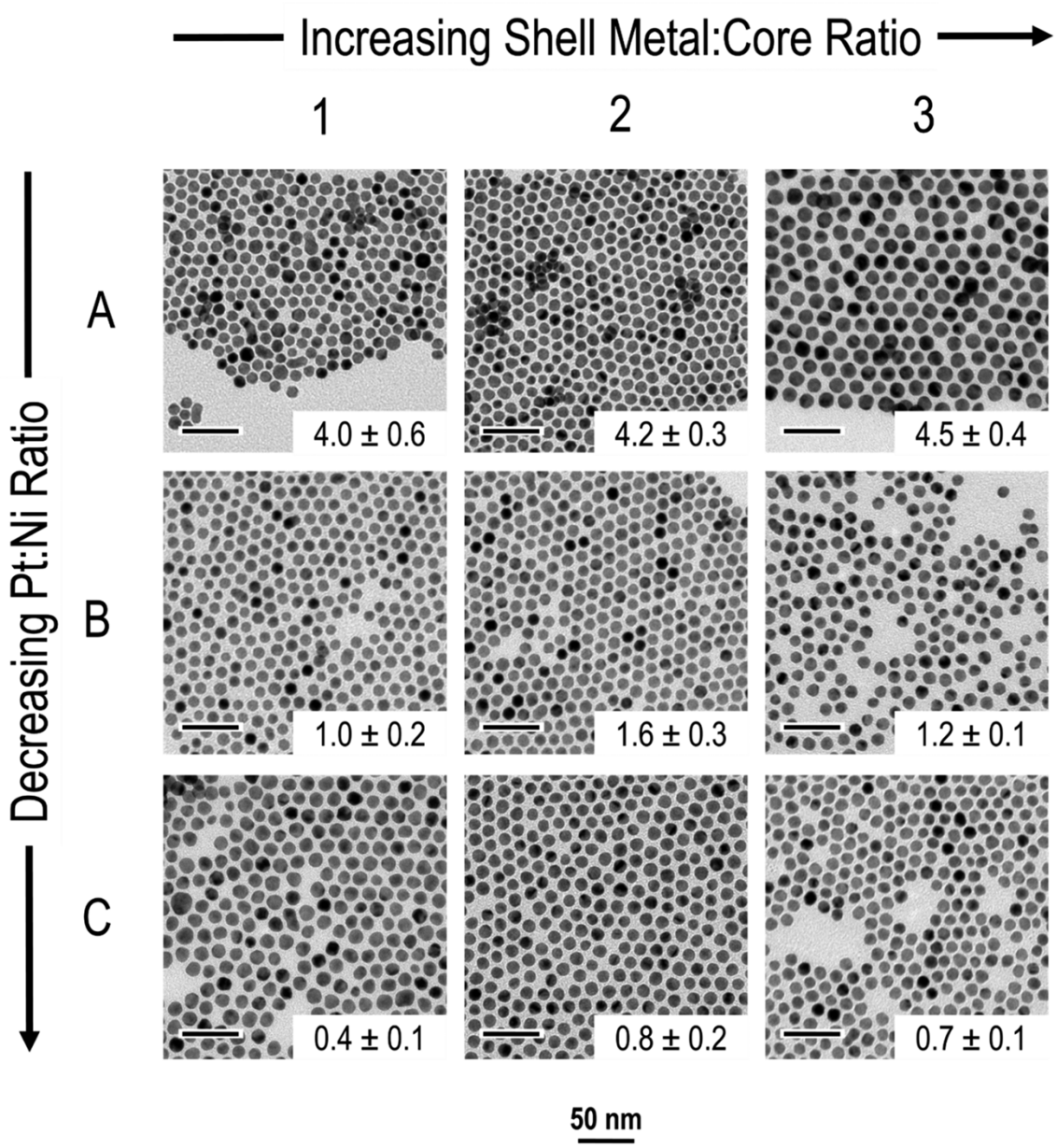

Figure 1. TEM images of PdCu B2@PtNi are shown for varying shell thickness and Pt:Ni ratios. Shell thickness increases from column 1 to 3, where the seed to initial shell metal precursor molar ratio was 1:2, 1:1, and 2:1, respectively. Rows A-C correspond to where the Pt:Ni molar ratio was varied from 3:1, 1:1, and 1:3, respectively. The inset of each TEM image is the Pt:Ni ratio determined by SEM-EDX.

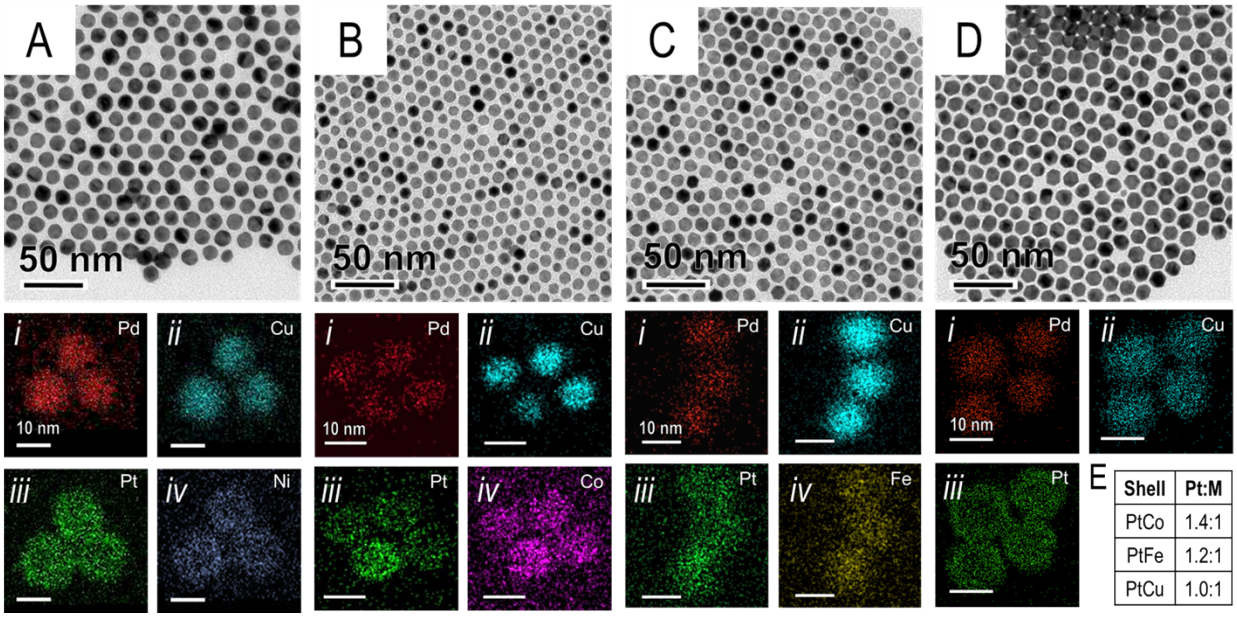

Figure 2. TEM images for PdCu B2@PtM (where M = Ni, Co, Fe, and Cu for **A, B, C, and D**, respectively) are shown. Under each TEM image is the STEM-EDX results **(*i-iv*)** for the listed samples. **(E)** Chart of the Pt:M ratios for each sample determined by SEM-EDX.

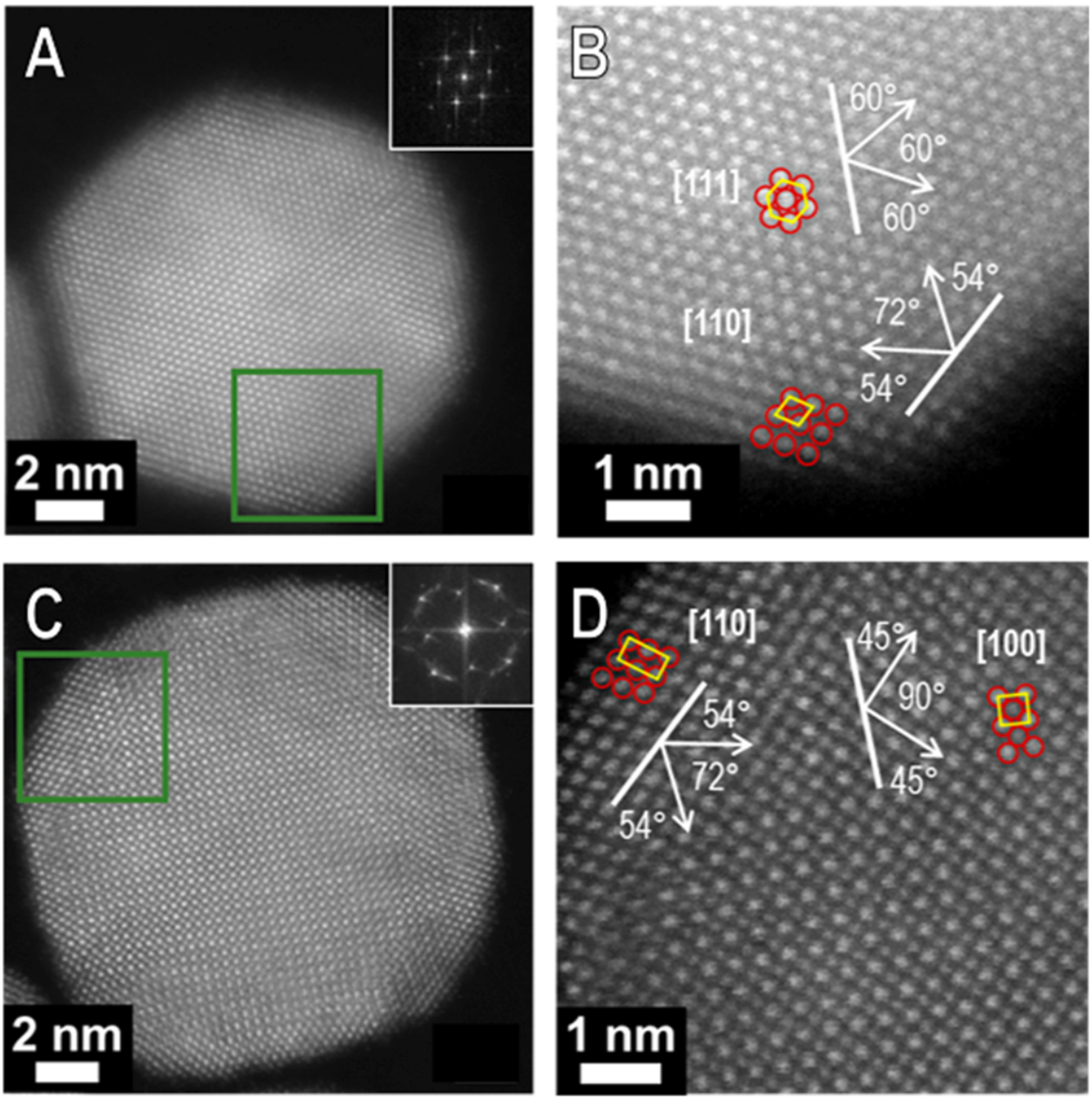

Figure 3. HAADF-STEM images along **(A-B)** [111] and **(C-D)** [100] zone axes of the NP core for samples A1 and A3, respectively. Parts **B** and **D** correspond to the regions boxed in green in parts **A** and **C,** respectively.

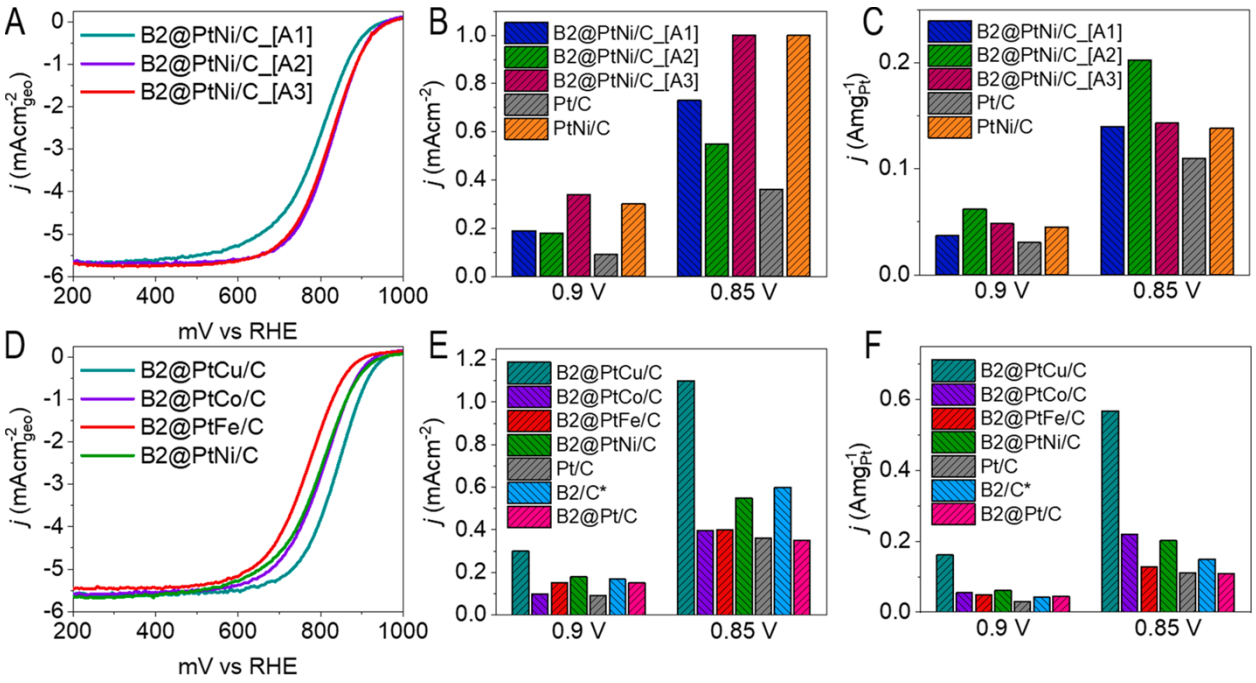

Figure 4. Polarization curves collected in O_2-saturated 0.1 M $HClO_4$ for **(A)** PdCu B2@PtNi with different shell thickness ([A1]/C 0.12, [A2]/C 0.25, and [A3]/C 1 nm shell thickness) and corresponding **(B)** specific and **(C)** mass activities. The polarization curves collected in O_2-saturated 0.1 M $HClO_4$ for the various **(D)** PdCu B2@PtNi/C (where M = Ni, Fe, Co, Cu) and the **(E)** specific and **(F)** mass activities. Sample [A2]/C was used for reference in parts **D-F** due to the shell thickness that is similar to those of the other samples. The B2/C catalyst is from previously reported data, and its mass activity is normalized by Pd loading.[37]

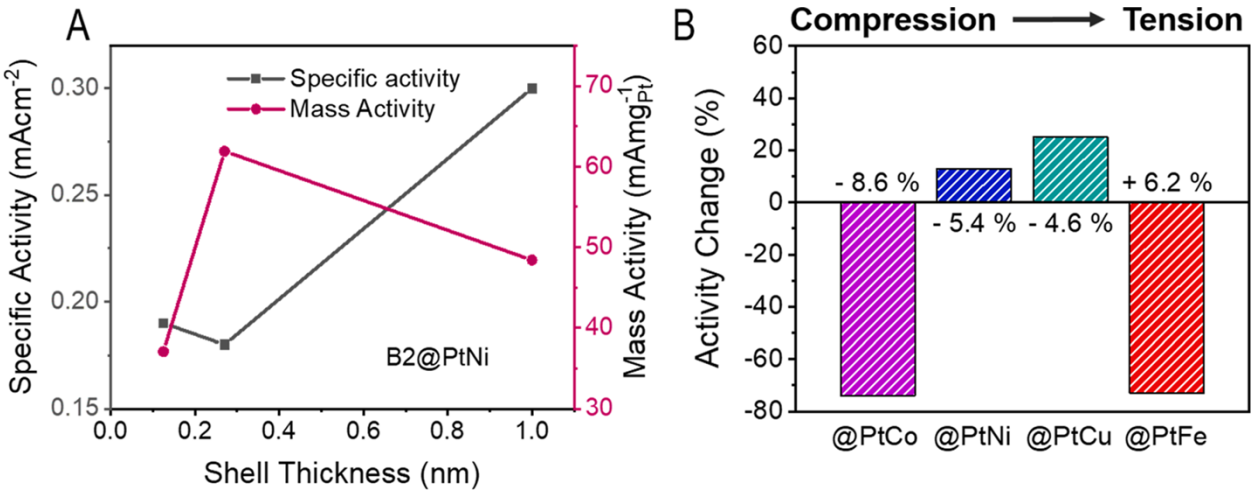

Figure 5. (A) Plot of specific and mass activities measured as a function of shell thickness for the PdCu B2@PtNi/C catalysts. **(B)** A bar graph summarizing the specific activity changes from the PdCu B2@PtM/C catalysts, where the activity change is the percent difference between specific activities of the core@shell catalysts and the PtM reference, where the percentages above each column represent the calculated lattice mismatch between core and shell.